Journal of Physics and Chemistry of Solids 111 (2017) 335–342

Contents lists available at ScienceDirect

Journal of Physics and Chemistry of Solids

journal homepage: www.elsevier.com/locate/jpcs

Homogeneously dispersed CeO_2 nanoparticles on exfoliated hexaniobate nanosheets

Thalles M.F. Marques [a], Megan E. Strayer [b], Anupama Ghosh [c], Alexandre Silva [c], Odair P. Ferreira [d], Kazunori Fujisawa [e], Jose R. Alves da Cunha [f], Guilherme J.P. Abreu [g], Mauricio Terrones [e], Thomas E. Mallouk [b], Bartolomeu C. Viana [c,h,*]

[a] Instituto Federal de Educação, Ciência e Tecnologia do Piauí – IFPI, 64760-000, Campus São João do Piauí-PI, Brazil
[b] Department of Chemistry, The Pennsylvania State University, University Park, PA, 16802, USA
[c] Departamento de Física, Universidade Federal do Piauí – UFPI, 64049-550, Teresina, PI, Brazil
[d] Laboratório de Materiais Funcionais Avançados (LaMFA), Departamento de Física, Universidade Federal do Ceará - UFC, 60440-554, Fortaleza, CE, Brazil
[e] Department of Physics and Center for 2-Dimensional and Layered Materials, The Pennsylvania State University, 16802, University Park, PA, USA
[f] Faculdade de Ciências Exatas e Naturais, Universidade Federal do Pará, Campus Universitário de Tocantins, Cametá, PA, 68.400-000, Brazil
[g] Departamento de Física, Universidade Federal do Paraná - UFPR, 80060-000, Curitiba, PR, Brazil
[h] Pós Graduação em Ciências dos Materiais, Centro de Tecnologia, 64049-550, Teresina, PI, Brazil

ARTICLE INFO

Keywords:
Hexaniobate nanosheet
Support decoration
CeO_2 nanopartcles
Hybrid nanosystem

ABSTRACT

Hexaniobate nanosheets derived from the parent compound $K_4Nb_6O_{17}$ have been decorated with CeO_2 nanoparticles by ion exchange with aqueous cerium (IV) solution. Very homogeneous CeO_2 nanoparticle decoration of the hexaniobate sheets can be achieved by this method and the resulting composites may absorb visible light. HRTEM images show that ~3.0 nm diameter CeO_2 nanoparticles adhere to hexaniobate nanosheets that are exfoliated and then restacked prior to Ce deposition. The interfacial interaction between CeO_2 nanoparticles and nanosheets would be due to an electrostatic attraction mechanism. Raman and XRD measurements have given strong evidence that CeO_2 nanoparticles have fluorite structure. EDS, FTIR and XPS results suggest almost complete exchange of TBA^+ and K^+ by Ce^{4+}. Cerium ion exchange on the acid exchanged parent compound, $H_{2.9}K_{1.1}Nb_6O_{17}$, revealed that the extent of Ce ion exchange is much greater in case of nanosheets, which may be rationalized by the larger surface area available after exfoliation. XPS measurements show that the ratio of Ce^{4+}/Ce^{3+} is around 4.4, in agreement with the formation of fluorite structure (CeO_2). Thus, these CeO_2 nanoparticle/nanosheet composites may be useful for catalytic processes.

1. Introduction

Synthesizing new functional materials with control over structure, morphology and dimensionality and tailoring them for different applications is an important goal of materials science. Bi-dimensional and one-dimensional structures has been very intensively studied and are useful because of their surface area, hosting ability and particular electronic properties [1]. Along with carbon nanotubes, graphene and various organic supra-molecular tubular and planar structures, different inorganic uni- and bi-dimensional materials have been explored for their tunable properties and adequate applications. Amongst them, lamellar transition metal oxides are very intriguing because of their protonic and electronic conductivity, dielectric properties, and electronic interactions with catalytic metal nanoparticles [2]. These layered materials can be exfoliated into thinner layers with the aid of intercalation by aqueous solution of organic bases [3,4] or other adequate organic molecules [5,6] to achieve properties different from their bulk counterparts [7].

Among these oxides, $K_4Nb_6O_{17}$ is unusual in that the asymmetric sheets are stacked alternately in a head-to-head and tail-to-tail fashion in the crystal structure [8]. This structural feature enables selective intercalation of two chemically distinct interlayer galleries, a property that has been exploited for photocatalysis [9] and for exfoliation to produce either bilayer flat sheets or nanoscrolls [10,11]. Very recently Hu et al. have carefully designed a partial protonation and restacking method to obtain nanoscrolls and nanosheets of $K_4Nb_6O_{17}$, both of which showed enhanced photocatalytic property, owing to their high surface area [12].

* Corresponding author. Departamento de Física, Universidade Federal do Piauí – UFPI, 64049-550, Teresina, PI, Brazil.
E-mail address: bartolomeu@ufpi.edu.br (B.C. Viana).

http://dx.doi.org/10.1016/j.jpcs.2017.08.027
Received 19 May 2017; Received in revised form 7 August 2017; Accepted 18 August 2017
Available online 19 August 2017

These nanoscrolls can be further processed by thermal dehydration [13] or decoration and/or functionalization with other active moeities [14, 15] such as metal and metal oxide particles owing to the thermodynamically favorable interfacial interaction energy [16]. Furthermore, these layered materials can be used as an metal ion scavengers to remove pollutants from water [17,18].

Metal ion exchange on tubular or lamellar inorganic structures by simple chemical routes has been established as an easy and useful way of generating functional hybrid materials [19–22]. For example, improving catalytic properties because of band gap engineering in case of photocatalysis [23–25], or modulating Lewis and Brønsted acidity/basicity [26] in case of heterogeneous catalysis. $K_4Nb_6O_{17}$ has been exfoliated and acid exchanged in order to realize increased photocatalytic activity [27]. Additionality, partial or total metal ion exchange with Fe^{3+}, Ce^{3+}, Cu^{2+} and Ag^{+} can lead to enhanced photo- or heterogeneous catalysis, and the thermal treatment of these ion-exchanged products can generate composite nanostructures [28–30].

Ce ion doping of transition metal oxides can lead to modified electronic [31] and catalytic properties [32]. CeO_2 (Ceria) is important oxide due to its applications as an active catalyst in vehicle emission systems, as a solid oxide ion conductor, as a fuel cell electrode material, as the active material in gas sensors, and as a component of high T_C-superconductors [33–37]. The catalytic properties of nanoscale ceria are enhanced by its high surface-to-volume ratio, and hybrid materials have been generated by growing CeO_2 nanoparticles in solid solutions [38]. Viana et al. have been successful in decorating titanate nanotubes with very small (3–4 nm) CeO_2 nanoparticles by a simple ion-exchange process with ammonium cerium (IV) nitrate solution, ending up with different band gap for the hybrid system and increased solar photocatalytic activity in the degradation of dyes [39]. CeO_2-titanate nanostructures have also been synthesized by hydrothermal or other methods [31–33,40–42] with useful catalytic properties [43–46]. The study of the growth of CeO_2 nanoparticles on the external walls of titanate nanotubes suggested that a simple ionic interaction is responsible for the attachment of the nanoparticles to the anionic walls of the tubes [47–51]. Other hybrid systems, like hydrous cerium oxide (HCO)-Graphene platelet composites, have been obtained by simple stirring. These materials can capture arsenate ions through bonding with OH groups on HCO, which are distributed uniformly over the graphene sheets [52]. Although there are reports on the structure and properties of bulk and nano-structured cerium niobate which can have an variety of applications [53–57], few studies have been done on cerium ion exchange of two-dimensional metal oxide nanosheets.

In this work, we have performed a simple cerium ion exchange reaction using aqueous ammonium cerium (IV) nitrate solution on exfoliated and restacked potassium hexaniobate (R-$K_4Nb_6O_{17}$) sheets. It has been found that along with the cerium ion exchange, very small CeO_2 nanoparticles form in the solution and are bonded to the hexaniobate nanosheets surface to give rise to a new homogeneous hybrid functional material. Careful microscopic (TEM, HRTEM and SEM), XRD and spectroscopic (Raman, EDS and XPS) characterizations suggest the decoration of small (~3.0 nm) CeO_2 nanoparticles (fluorite structure) over hexaniobate sheets mainly by a strong electrostatic interaction between the nanoparticles (positively charged) and nanosheets (negatively charged). In addition, XPS study indicates that the CeO_2 nanoparticles have been performed with oxygen vacancies, which may be useful for catalytic processes [58].

2. Experimental section

2.1. Synthesis

1$H_{2.9}K_{1.1}Nb_6O_{17}$ preparation

The layered metal oxide $K_4Nb_6O_{17}$ was synthesized by heating K_2CO_3 and Nb_2O_5 (sigma-aldrich) at 1100 °C for 24 h as described in earlier literature [13]. The as-obtained solid (1.0 g) was then proton exchanged by mixing with 100 mL of 1.0 mol/L HNO_3 for three days and exchanging the acid solution daily. The suspension was centrifuged and the solid product was washed with deionized water and centrifuged again one more time. The powder obtained ($H_{2.9}K_{1.1}Nb_6O_{17}$) was then dried at 80 °C.

2Exfoliated/Restacked $K_4Nb_6O_{17}$ nanosheet preparation (R-$K_4Nb_6O_{17}$)

The $H_{2.9}K_{1.1}Nb_6O_{17}$ (0.100 g) was stirred in 50 mL of tetra-*n*-butylammonium hydroxide (TBA^+OH^-, Alfa Aesar) aqueous solution (25 mmol/L) overnight or longer to complete the exfoliation reaction. The pH of the solution after exfoliation was 12 and the unexfoliated material was allowed to settle overnight. After decanting the unexfoliated sample, the material was restacked by adding the suspension dropwise into 2 M KOH (50 mL). This sample was named as R-$K_4Nb_6O_{17}$.

3Cerium ion exchange/decoration process.

Cerium ion-exchange/decoration reaction was carried out with R-$K_4Nb_6O_{17}$ nanosheets and $H_{2.9}K_{1.1}Nb_6O_{17}$ samples by suspending 100 mg of each sample separately in 100 mL of 0.05 mol/L aqueous solutions of $(NH_4)_2Ce(NO_3)_6$ (sigma-aldrich). The suspensions had initial pH equal to 4 and they were stirred with the aid of a magnetic stirrer for 24 h at room temperature (at about 25 °C). The solid product was isolated by centrifugation at 3500 rpm, and it was washed several times with deionized water, until the final supernatant pH reach 7 (the initial pH was 4). Washing removes remaining soluble ions such as TBA^+, K^+, OH^-, Ce^{4+}, NH_4^+ and NO_3^-. The solid product was then vacuum-dried to obtain the Ce-$K_4Nb_6O_{17}$ sheets (from R-$K_4Nb_6O_{17}$) and the Ce-$H_4Nb_6O_{17}$ plates (from $H_{2.9}K_{1.1}Nb_6O_{17}$). Both of them have a yellow coloration due to cerium incorporation (visible light absorption). However, as shown in Fig. S1, the yellow color of Ce-$K_4Nb_6O_{17}$ sheets is much more intense (Fig. S1(a)) than the Ce-$H_4Nb_6O_{17}$ plates (Fig. S1(b)), see supplementary information), probably due to the higher extent of cerium ion exchange onto the exfoliated sheet than onto the unexfoliated plates.

2.2. Characterizations

Fourier transform infrared (FTIR) spectroscopy was recorded using an attenuated total reflectance (ATR) setup in a Vertex 70 spectrometer (Bruker company). A total of 64 scans and a resolution of 4 cm^{-1} were used for obtaining spectra with good signal-to-noise ratios. The range used was 600–4000 cm^{-1}.

Raman spectroscopy experiments were performed on a confocal Raman spectrometer, Bruker Senterra, with a 50× objective and 785 nm laser as the excitation source. Low laser power density was used in order to avoid sample overheating. A spectral resolution of 3 cm^{-1} was used and the range employed was 80–1050 cm^{-1}. Also, Raman spectroscopy was performed using a Renishaw inVia confocal micro-Raman spectrometer in the wavenumber range (100-3200 cm^{-1}) with a 100× objective of confocal microscope and 514 nm laser as the excitation source; the spectral resolution was 2 cm^{-1}.

X-ray powder diffraction (XRD) patterns were obtained with a Shimadzu XRD6000 diffractometer using Cu Kα ($\lambda = 1.5406$ Å) radiation operating at 30 mA and 40 kV. A scan rate of 1° min^{-1} was used and the 2θ range was 5–70°.

Scanning electron micrographs (SEM) were collected using a FEI Quanta FEG250 microscope. Elemental (qualitative) analysis by energy dispersive spectroscopy (EDS) was performed using an EDAX Apollo X probe attached to the SEM. The powdered samples were dispersed onto carbon tape placed on the SEM sample holder.

Transmission electron microscopy (TEM) images were obtained using a JEOL-JEM-2010F microscope operating at 200 keV. The samples were prepared by the dropping of an aqueous suspension of sample powder

onto a holey carbon-coated copper grid and letting the water evaporate at room temperature.

XPS spectra were collected on a VSW HA-100 spherical analyzer instrument using MgKα radiation (hv = 1253.6 eV). High-resolution spectra were measured with a constant analyzer pass energy of 44 eV, which produced a full width at half-maximum (FWHM) line of 1.6 eV for the Au($4f_{7/2}$) peak. The calibration of the binding energy and the corrections of the energy shift as a result of the steady-state charging effect were accomplished by assuming that the C 1s line is centered at 284.6 eV.

Zeta potential measurements (10 times for each sample) were performed in the aqueous suspensions of the samples, using a Malvern - Zetasizer nanoZS - instrument.

3. Results and discussion

The Raman spectra of R-$K_4Nb_6O_{17}$ sheets and cerium-exchanged Ce-$K_4Nb_6O_{17}$ sheets are shown in the lower and upper traces of Fig. 1 (a) respectively. Apparently, the addition of the Ce^{4+} ions to the hexaniobate sheets does not substantially alter the Nb-O stretching vibrations and lattice modes of the hexaniobate sheets, as the Raman spectra do not show any significant change. However, some changes could be highlighted, first, the typical vibrational mode of CeO_2 crystalline phases at 460 cm^{-1} appears in the Raman spectrum of Ce-$K_4Nb_6O_{17}$. Thus, this result suggests that CeO_2 nanoparticles are grown over the hexaniobate sheets and are likely to have the fluorite structure, belonging to *Fm3m* space group which has a Raman active T_{2g} (assigned in Fig. 1(a)) mode at around 460 cm^{-1}. Second, vibrational modes of the hexaniobate sheets around 200 cm^{-1} (lattice mode) and 890 cm^{-1} (Nb - O terminal stretching mode of highly distorted NbO_6 octahedra) have undergone a slight blue-shift after Ce^{4+} ion exchange, because of the change in Nb - O bond energy when Ce^{4+} is substituted for K^+, and the intensity of the bands near 386 cm^{-1} and 645 cm^{-1} (Nb - O vibrations of slightly distorted octahedra) decrease the intensity with Ce^{4+} ion intercalation [59] The Raman spectra of unexfoliated $H_{2.9}K_{1.1}Nb_6O_{17}$ plates and Ce-$H_4Nb_6O_{17}$ plates are shown in the lower and upper traces of supplementary Fig. S2(a) (see supplementary information), respectively. Also, no significant changes are found in these spectra, and no characteristic peaks of CeO_2 are observed, probably due to the lower extent of Ce^{4+} ion exchange. ATR-FTIR spectra of R-$K_4Nb_6O_{17}$ sheets and Ce-$K_4Nb_6O_{17}$ sheets are shown in the lower and upper traces, respectively, of Fig. S3. ATR-FTIR spectra of the samples show similar characteristics in the Nb-O stretching region between 1000 and 700 cm^{-1}. The band located at 877 cm^{-1} is ascribed to the stretching vibration of Nb-O terminal groups; the broadening of the band and the shift to lower energy derive from a decrease in the number of terminal ligands owing to their gradual Ce ion exchange. The asymmetric Nb-*O*-Nb stretching vibration is found near 795 cm^{-1}. Both spectra show a strong and broad band at around 3300 cm^{-1} (Fig. S3), which is attributed to the O-H stretching mode of hydroxyl groups and structural/adsorbed water. The intensity of the water and surface-hydroxyl bands is decreased as Ce^{4+} intercalation. This can be interpreted in terms of the formation of CeO_2 on the surface of hexaniobate sheets, which involves an ionic linkage with the negatively charged surface of sheets, thereby displacing protons and decreasing the intensity of the O-H bands. A similar result was found in case of Ce^{4+} ion-exchange of titanate nanotubes [51]. The presence of TBA^+ ions is characterized by bands around 2800–3000 cm^{-1} assigned to C-H stretching, and at around 1470 and 1380 cm^{-1}, which are attributable to the bending and deformation modes of the CH_2 group, respectively [60]. Also, it can be seen a decrease of the intensity, probably, due to partial substitution of TBA^+ by Ce^{4+}.

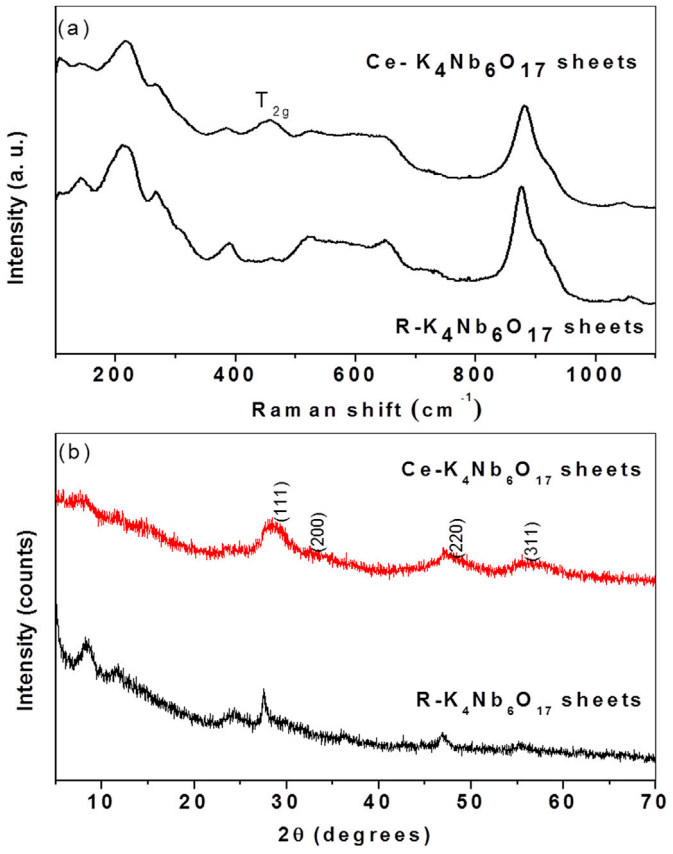

Fig. 1. (a) Raman spectra of R-$K_4Nb_4O_{17}$ sheets and Ce-$K_4Nb_4O_{17}$ sheets, taken with 785 nm laser, Ce-$K_4Nb_4O_{17}$ sheets shows the CeO_2 related peak at around 460 cm^{-1}. (b) XRD pattern of R-$K_4Nb_6O_{17}$ sheets and Ce-$K_4Nb_6O_{17}$ sheets showing the main CeO_2 (fluorite structure) crystalline planes.

The X-ray powder diffraction patterns of R-$K_4Nb_6O_{17}$ sheets and Ce-$K_4Nb_6O_{17}$ sheets are shown in the lower and upper traces of Fig. 1 (b), respectively. Broad, low intensity diffraction peaks are observed for both samples, consistent with the lack of long range order in the scrolled and exfoliated nanosheets. A broad peak at around 8.4° is related to the basal spacing (040) of hexaniobate sheets and broad peaks at around 24° and 17.5° can be indexed as planes (2 0 0) and (0 0 2) of hexaniobate sheets [10,61]. After Ce^{4+} exchange, the XRD pattern remains essentially the same suggesting retention of the lamellar structure although the peak around 8.4° broadens with Ce^{4+} incorporation. Similar phenomena have previously been observed with Rh deposition onto hexaniobate sheets [14]. However, after Ce^{4+} exchange, new shoulder-like peaks at 33°, 48° and 58° (2θ) appear, which can be assigned to the (200), (220) and (311) diffraction planes of the fluorite CeO_2 structure respectively, as reported previously [47] and further confirmed by TEM analysis. In addition, in the diffractogram of the Ce-$K_4Nb_6O_{17}$ sample it can be observed that the relative intensity of different peaks is changed and peaks are broader and more asymmetric if compared to diffractogram of raw material. This behavior could be related to the changes in environment due to the ion exchange of Ce^{4+} and/or CeO_2 nanoparticle deposition. A similar phenomenon has been observed in the case of titanate nanotubes [39]. The broadening and asymmetry of the hexaniobate diffraction peaks after Ce^{4+} deposition suggests a disordered chemical environment due to the ion-exchange. The average size of CeO_2 nanoparticles can be estimated from XRD peak analysis using the Scherrer equation. Only the (311) diffraction peak was used in the calculation, as it is most prominent. The average particle size was found to be 3.5 nm. The XRD diffraction patterns of unexfoliated $H_{2.9}K_{1.9}Nb_6O_{17}$ plates and Ce-$H_4Nb_6O_{17}$ plates are shown in the lower and upper traces of Fig. S2(b) respectively. They show practically no difference from one another, which can be attributed to the fact that the amount of Ce^{4+} exchange is quite small and the changes are not so prominent due to the bulk-nature of the sample.

Fig. 2(a) presents a scanning electron image of R-$K_4Nb_6O_{17}$ sheets. This image clearly shows the sheet-like morphology with a small amount of scroll-like structures. Meanwhile, The samples were washed in order to lower the amount of organic cations and other superficial ions. This

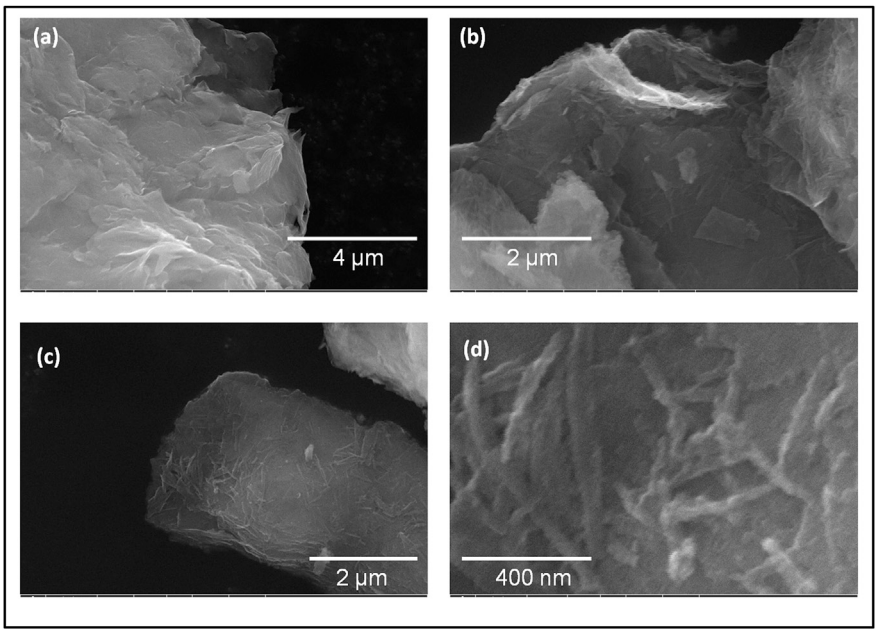

Fig. 2. SEM micrographs of (a) R-$K_4Nb_4O_{17}$ sheets and (b), (c) of Ce-$K_4Nb_4O_{17}$ sheets. (d) Higher magnification SEM image of Ce-$K_4Nb_4O_{17}$ sheets which shows scroll-like structures.

procedure decreases the solution ionic strength and under these conditions the formation of hexaniobate tubes is not favorable [61]. On the other hand, in Fig. 2(b) and (c), sheet-as well as scroll-like structures derived from Ce-$K_4Nb_6O_{17}$ sheets can be clearly observed. Fig. 2(d) shows a high resolution image of Ce-$K_4Nb_6O_{17}$ sheets with clear view of nano-scrolls. It is evident that the sheet-like hexaniobate structures are being rolled up when subjected to Ce^{4+} ion exchange. This can be explained in the terms of change density of Ce^{4+}. With smaller size and high charge density, when one Ce^{4+} ion replaces four H^+ ions, the flat hexaniobate sheet with surface negative charges due to surface O-H groups rolls up in order to avoid the charge repulsion and larger amounts of nanoscrolls are formed. Energy dispersive X-ray spectroscopy (EDS) analyses were also performed along with SEM in order to infer about the chemical composition of the R-$K_4Nb_6O_{17}$ after Ce^{4+} ion exchange as shown in Table 1. However, EDS measurements have not determined the exact Ce content of the exchanged phase. It shows a very efficient ion-exchange as all K^+ ions have been replaced by Ce^{4+} ions. Furthermore, the Ce/Nb ratio is much higher than the K/Nb ratio after the ion exchange because the Ce signal also comes from the CeO_2 nanoparticles, which decorate the nanotubes. To confirm and elucidate these results, transmission electron microscopy was performed on all the samples.

Fig. 3(a) shows a low-magnification TEM image of R-$K_4Nb_6O_{17}$ nanosheets which reveals the thin sheet-like structures with occasional needle-like formation indicating a tubular morphology. The dimensions of these tubes matches with previous reports [15], and some of them consist of two tubes joined together in a parallel orientation, which suggests that the tubes are formed by scrolling of the opposite edges of one hexaniobate sheet. Thus, they are hexaniobate sheets containing curled opposite edges. Also, it could be inferred that the neutralization of excess of negative charges on exfoliated samples favors sheet curling [13, 61]. Fig. 3(b) shows the clear sheet-like morphology as the HRTEM image shown in Fig. 3(c) reveals the crystalline nature of the sheet with two lattice parameters at around 0.31 nm and 0.36 nm. Fig. 3(d) shows a low-magnification, large-area image of Ce-$K_4Nb_6O_{17}$ (from R-$K_4Nb_6O_{17}$) with a mixture of exfoliated nanosheets and nanoscrolls. Fig. 3(e) and (f) show the presence of nanoscrolls, while Fig. 3(g) shows a sheet-like morphology, and all of them are homogeneously decorated with very small nanoparticles. Fig. 3(h) and (i) show images containing higher resolution images of these nanoparticles, and an HRTEM image of these particles is shown in Fig. 3(j). Nanoparticles have a *d*-spacing of 0.31 nm which is indexed to the (111) plane of CeO_2 with the fluorite structure as suggested by the XRD analysis. In Fig. 3(k) a histogram of average particle size analysis is shown and an average diameter of the CeO_2 nanoparticles at around 3.4 nm is found (0.7 nm of standard deviation). Thus, the physical dimensions of the CeO_2 nanoparticles are in very good agreement with XRD linewidth results. The TEM and HRTEM images of $H_{2.9}K_{1.1}Nb_6O_{17}$ plates and Ce-$H_4Nb_6O_{17}$ plates are shown in Fig. S4. Fig. S4(a) and (b) reveals the thick plate-like morphology of $H_{2.9}K_{1.1}Nb_6O_{17}$ sample with lattice parameter of 0.41 nm (Fig. S4(c)). After the Ce^{4+} ion exchange the plate-like morphology is retained as seen in Fig. S4(d), but these plates also present CeO_2 nanoparticles homogeneously dispersed on their surface (Fig. S4 (e, f, g)). The HRTEM images (Fig. S4(h) and(i)) are indicanting nanoparticles with *d*-spacing of 0.31 nm which can be indexed to the (111) plane of fluorite-structure of CeO_2. In Fig. S4(j), a histogram of average particle size shows that the average diameter of the CeO_2 nanoparticles is 2.8 nm (0.4 nm of standard deviation).

XPS measurements were performed to check the sample stoichiometry and determine the cerium oxidation state. Fig. 4(a) shows survey spectra, which indicate that there is a significant amount of Ce on the R-$K_4Nb_6O_{17}$ nanosheets, probably covering the sheet surface, in comparison with the lower relative amount of the other elements. The complete ion exchange of the K^+ ion by Ce^{4+} ions due to the drastic decrease of the K2p peaks. Integration of peaks in the XPS spectra enabled the determination of the surface concentrations of the elements, as shown in Table 2 [62].

Fig. 4(b) shows the Nb3d spectra for R-$K_4Nb_6O_{17}$ and Ce-$K_4Nb_6O_{17}$

Table 1
Elemental composition from EDS mapping analysis of R-$K_4Nb_6O_{17}$ and Ce-$K_4Nb_6O_{17}$ sheets.

Element	Sample	
	R-$K_4Nb_6O_{17}$ sheets (atomic percentage)	Ce-$K_4Nb_6O_{17}$ sheets (atomic percentage)
O	69.5	67.2
Nb	20.1	21.3
K	9.4	0.0
Ce	0.0	11.4

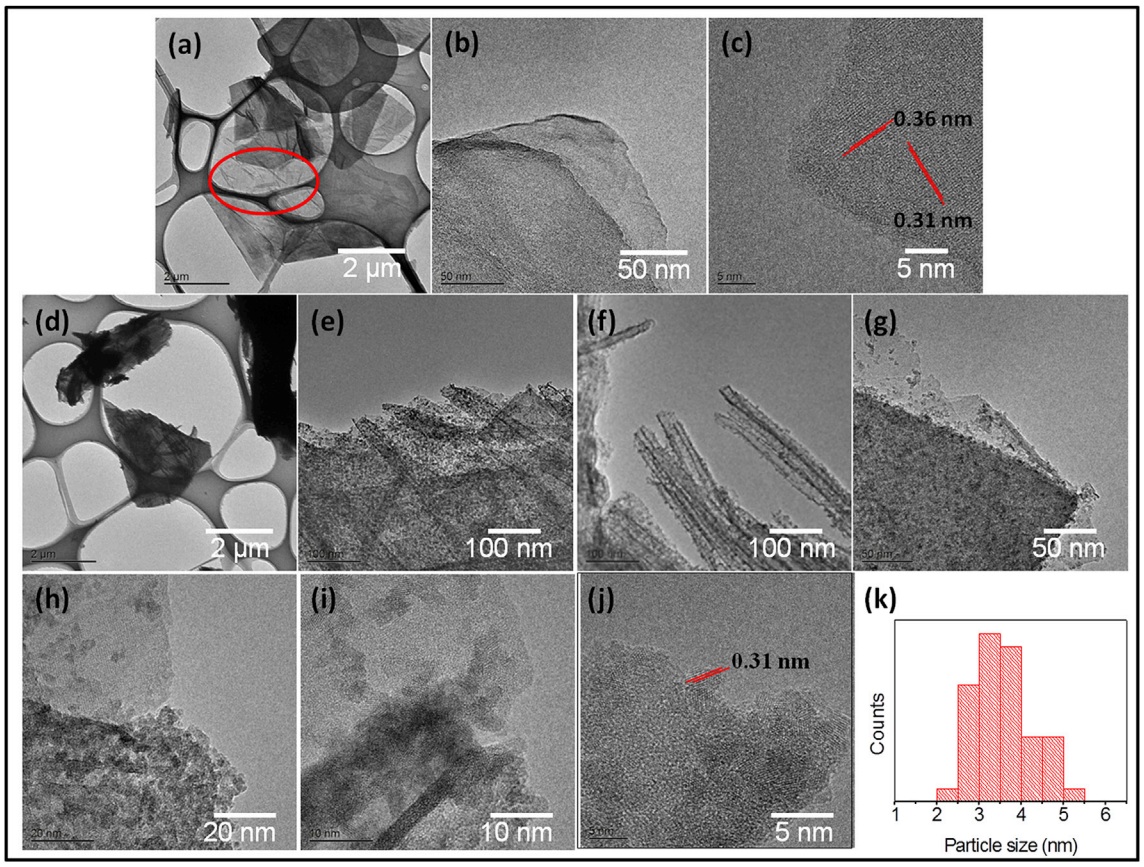

Fig. 3. TEM images of R-$K_4Nb_6O_{17}$ sheets (a) low magnification, (encircled area shows the presence of tube or scroll like structures); (b) high magnification and (c) HRTEM images of Ce-$K_4Nb_6O_{17}$ sheets in (d) low magnification and (e)–(i) high magnification; In (e) and (f) the tube or scroll type of structures can be located on the edge of the sheets; In (g), (h) and (i) it could clearly see the CeO_2 nanoparticles; (j) shows the average diameter distribution of the particles with average size of ~3.4 nm; (k) shows the HRTEM of the sample, with d spacing of (111) plane CeO_2 particle as 0.31 nm.

sheets. Spectral fitting indicates two chemically different Nb environments with a binding energy difference of 2.8 eV, as reported in the literature [63–65]. In addition, the fitting parameters indicate a spin-orbit splitting between the $Nb3d_{5/2}$ and the $Nb3d_{3/2}$ peaks of 3.1 eV for R-$K_4Nb_6O_{17}$ nanosheets and of 2.6 eV for Ce-$K_4Nb_6O_{17}$ nanosheets. The results are in good agreement with standard samples and the resolution of the equipment. Fig. 4(c) exhibits the O1s spectra for the R-$K_4Nb_6O_{17}$ and Ce-$K_4Nb_6O_{17}$ sheets. The spectra were fit to two peaks separated by 1.8 eV (R-$K_4Nb_6O_{17}$) and 1.9 eV (Ce-$K_4Nb_6O_{17}$). The origin of the second O1s peak (at around 530 eV) is not clear, but, it could be associated with vacancies in ceria or surface hydroxyl groups on the nanosheets [62]. Because the second peak appears even in the sample without Ce, it is reasonable to conclude that the second hypothesis is more likely. Fig. 4(d) shows the Ce 3d spectrum for the Ce-$K_4Nb_6O_{17}$ sheet sample. The fitting results indicate five sets of spin-orbit doublets. The peak of Ce $3d_{5/2}$ is line u and the peak of Ce $3d_{3/2}$ is the line v. The origin of each one of these peaks has widely studied in literature [66,67]. Lines u_0, u_1, v_0 and v_1 correspond to Ce^{3+}, whereas lines u, u_2, u_3, v, v_2 and v_3 correspond to Ce^{4+}. In order to estimate the oxidation state of Ce, the method of Romeo et al. can be applied [66]. The concentration of Ce^{3+} can be calculated using the Ce 3d fitting parameters, applying Equation (1).

$$\%Ce^{3+} = \frac{\nu_0 + \nu_1 + u_0 + u_1}{\nu_0 + \nu + \nu_1 + \nu_2 + \nu_3 + u_0 + u + u_1 + u_2 + u_3} \quad (1)$$

The results indicates a concentration of ~19% Ce^{3+} and 81% Ce^{4+} on the surface of the Ce-$K_4Nb_6O_{17}$ sheets.

In order to give insights about interaction mechanism between niobate nanosheets and CeO_2 nanoparticles, Zeta potential measurements were also carried out for R-$K_4Nb_6O_{17}$ nanosheets, Ce-$K_4Nb_6O_{17}$ nanosheets and $(NH_4)_2Ce(NO_3)_6$) solutions, showing average values of −56 mV, −12.3 mV and +11.8 mV, respectively. It was already demonstrated that Ce^{4+} ions can be hydrolyzed to CeO_2 colloidal nanoparticles (size of approximatively 3 nm) even in acid conditions (pH ~ 0.5) [49,51]. Thus, the previously formed CeO_2 nanoparticles could attach to the hexaniobate nanosheets, where they are strongly anchored by a simple electrostatic interaction. This fact could also explain the small size and narrow distribution of nanoparticles on hexaniobate nanosheets, as it was demonstrated in a similar system recently published [51], and also by the zeta potential measurements. Although there are other mechanisms proposed in the literature for the interaction between nanoparticles and niobate support such as covalent bonding [16], in the present case it is believed that the electrostatic interaction is the main mechanism since the CeO_2 nanoparticles were already previously formed and coexisting with Ce^{4+} ion in solution, before of the support addition (see experimental section).

4. Conclusion

In summary, efficient Ce^{4+} ion exchange has been carried out with exfoliated and restacked $K_4Nb_6O_{17}$ sheets, replacing almost all K^+ ions by Ce^{4+} ions. The ion exchange process does not destroy the basic morphology of the hexaniobate nanosheets, but incorporates some amount of scroll-like structures, the probable reason for this fact is the charge neutralization by Ce^{4+}. The pristine hexaniobate nanosheets not only underwent ion exchange and scrolling but also were uniformly

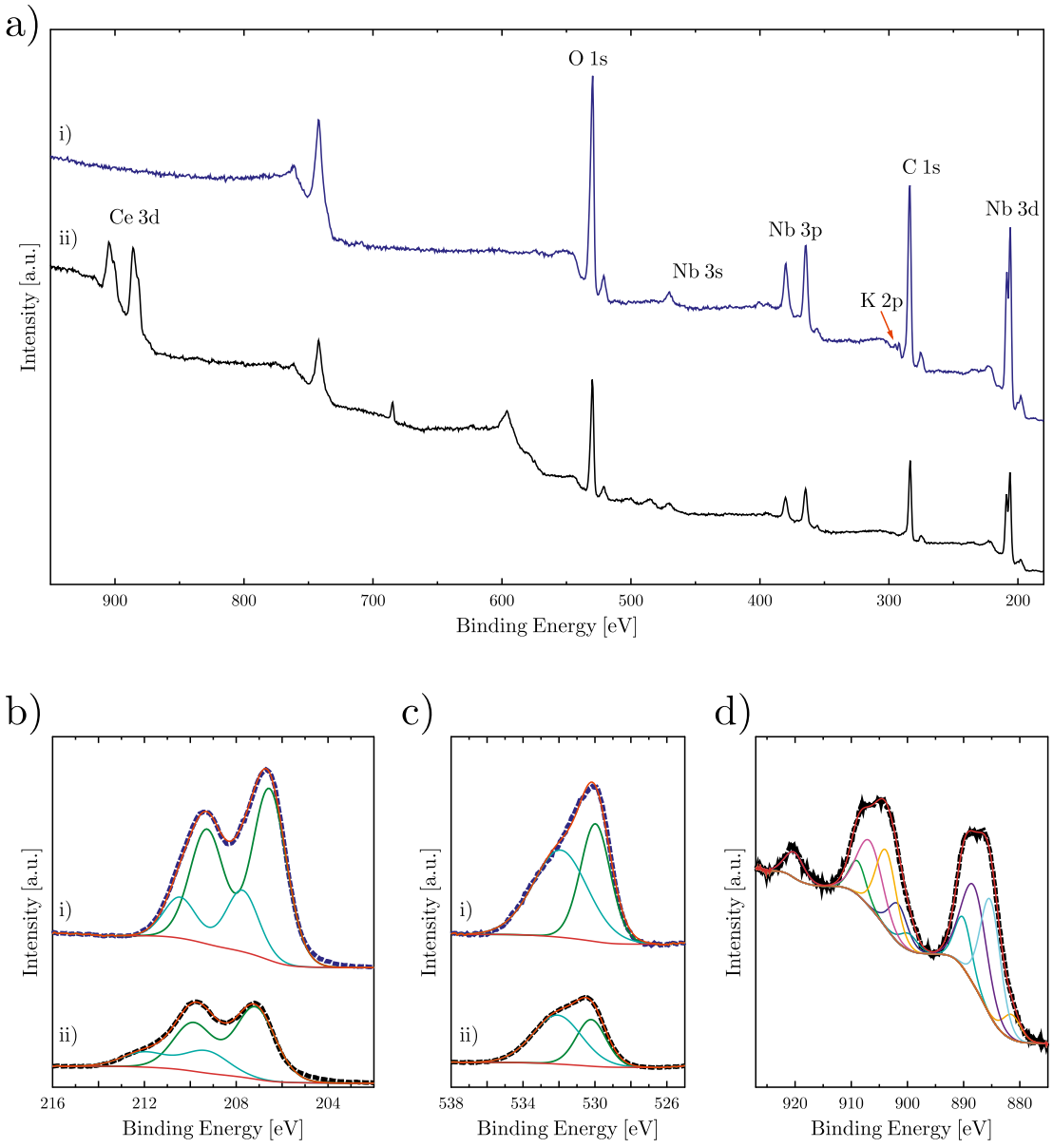

Fig. 4. a) XPS spectra of i) R-$K_4Nb_6O_{17}$ and ii) Ce-$K_4Nb_6O_{17}$ sheets, b) High resolution XPS Nb3d spectra of i) R-$K_4Nb_6O_{17}$ and ii) Ce-$K_4Nb_6O_{17}$ sheets, c) High resolution XPS O1s spectra of i) R-$K_4Nb_6O_{17}$ and ii) Ce-$K_4Nb_6O_{17}$ sheets and d) High resolution XPS Ce2p spectrum of the R-$K_4Nb_6O_{17}$sheets.

Table 2
Elemental composition from XPS spectra elemental analysis of R-$K_4Nb_6O_{17}$ and Ce-$K_4Nb_6O_{17}$ sheets.

Element	Sample	
	R-K4Nb6O17 sheets (atomic percentage)	Ce-K4Nb6O17 sheets (atomic percentage)
O	74.2	66.7
Nb	23.6	22.6
K	2.2	0.4
Ce	0.0	10.3

decorated by 3.0 nm diameter CeO_2 nanoparticles. XRD and TEM studies reveal that the CeO_2 nanoparticles are crystalline with the fluorite structure. The interfacial interaction between nanoparticles and support would be due to an electrostatic attraction mechanism. Similar ion exchange process occurs with proton-exchanged $H_{2.9}K_{1.1}Nb_6O_{17}$ plates, but the extent of the exchange is not high, probably due to the lower available surface area of the plates. Thus, exfoliation of lamellar $K_4Nb_6O_{17}$ and Ce ion exchange/CeO_2 deposition can lead to the formation of new hybrid inorganic material that has good prospects for applications in catalysis and related fields.

Acknowledgments

We acknowledge Prof. Richard Landers from Gleb Wataghin Physics Institute (UNICAMP-Brazil) for XPS measurements. M.E.S. and T.E.M. acknowledge support of this research by the National Science Foundation under grant DMR-1306938. B.C.V. acknowledge support from CNPq Grants 305632/2016-7, 400397/2014-5 and 209430/2013-3. B.C.V. and O.P.F. are grateful to support from CAPES-PROCAD 2013 Grant 183995.

Appendix A. Supplementary data

Supplementary data related to this article can be found at http://dx.doi.org/10.1016/j.jpcs.2017.08.027.

References

[1] S. Adireddy, T. Rostamzadeh, C.E. Carbo, J.B. Wiley, Particle placement and sheet topological control in the fabrication of Ag-hexaniobate nanocomposites, Langmuir, ACS J. surfaces colloids 31 (2015) 480–485, http://dx.doi.org/10.1021/la503775f.

[2] T.I. Draskovic, T. Wang, C.N. Henderson, T.E. Mallouk, Protonic and electronic conductivity of the layered perovskite oxides HCa2Nb3O10 and Ca4Nb6O19, Int. J. Hydrogen Energy 39 (2014) 4576–4580, http://dx.doi.org/10.1016/j.ijhydene.2014.01.017.

[3] T. Wang, C.N. Henderson, T.I. Draskovic, T.E. Mallouk, Synthesis, exfoliation, and electronic/protonic conductivity of the dion–jacobson phase layer perovskite HLa2TiTa2O10, Chem. Mater. 26 (2014) 898–906, http://dx.doi.org/10.1021/cm401803d.

[4] F. Hashemzadeh, Porous calcium niobate nanosheets prepared by an exfoliation–restacking route, Water Sci. Technol. 73 (2016) 1378–1386, http://dx.doi.org/10.2166/wst.2015.610.

[5] N. Kimura, Y. Kato, R. Suzuki, A. Shimada, S. Tahara, T. Nakato, K. Matsukawa, P.H. Mutin, Y. Sugahara, Single-and double-layered organically modified nanosheets by selective interlayer grafting and exfoliation of layered potassium hexaniobate, langmuir, ACS J. surfaces colloids 30 (2014) 1169–1175, http://dx.doi.org/10.1021/la404223x.

[6] Y. Nabetani, A. Uchikoshi, S. Miyajima, S.Z. Hassan, V. Ramakrishnan, H. Tachibana, M. Yamato, H. Inoue, Synthesis of double-wall nanoscrolls intercalated with polyfluorinated cationic surfactant into layered niobate and their magnetic alignment, Phys. Chem. Chem. Phys. 18 (2016) 12108–12114, http://dx.doi.org/10.1039/C6CP01547F.

[7] H. Yuan, M. Nguyen, T. Hammer, G. Koster, G. Rijnders, J.E. ten Elshof, Synthesis of KCa2Nb3O10 crystals with varying grain sizes and their nanosheet monolayer films as seed layers for piezoMEMS applications, ACS Appl. Mater. interfaces 7 (2015) 27473–27478, http://dx.doi.org/10.1021/acsami.5b09456.

[8] K. Nassau, J. Shiever, J. Bernstein, Crystal growth and properties of mica-like potassium niobates, J. Electrochem. Soc. 116 (1969) 348–353, http://dx.doi.org/10.1149/1.2411844.

[9] K. Domen, A. Kudo, A. Shinozaki, A. Tanaka, K.-i. Maruya, T. Onishi, Photodecomposition of water and hydrogen evolution from aqueous methanol solution over novel niobate photocatalysts, Journal of the Chemical Society, Chem. Commun. (1986) 356–357, http://dx.doi.org/10.1039/C39860000356.

[10] G.B. Saupe, C.C. Waraksa, H.-N. Kim, Y.J. Han, D.M. Kaschak, D.M. Skinner, T.E. Mallouk, Nanoscale tubules formed by exfoliation of potassium hexaniobate, Chem. Mater. 12 (2000) 1556–1562, http://dx.doi.org/10.1021/cm981136n.

[11] S.W. Keller, H.-N. Kim, T.E. Mallouk, Layer-by-Layer Assembly of intercalation compounds and heterostructures on surfaces: toward molecular“ beaker” epitaxy, J. Am. Chem. Soc. 116 (1994) 8817–8818, http://dx.doi.org/10.1021/ja00098a055.

[12] C. Hu, L. Zhang, L. Cheng, J. Chen, W. Hou, W. Ding, A comparison of H+-restacked nanosheets and nanoscrolls derived from K4Nb6O17 for visible-light degradation of dyes, J. Energy Chem. 23 (2014) 136–144 (14) 60128–5, http://doi.org/10.1016/S2095-4956.

[13] Y. Kobayashi, H. Hata, M. Salama, T.E. Mallouk, Scrolled sheet precursor route to niobium and tantalum oxide nanotubes, Nano Lett. 7 (2007) 2142–2145, http://dx.doi.org/10.1021/nl0708260.

[14] R. Ma, Y. Kobayashi, W.J. Youngblood, T.E. Mallouk, Potassium niobate nanoscrolls incorporating rhodium hydroxide nanoparticles for photocatalytic hydrogen evolution, J. Mater. Chem. 18 (2008) 5982–5985, http://dx.doi.org/10.1039/b812003j.

[15] K. Maeda, M. Eguchi, S.-H.A. Lee, W.J. Youngblood, H. Hata, T.E. Mallouk, Photocatalytic hydrogen evolution from hexaniobate nanoscrolls and calcium niobate nanosheets sensitized by ruthenium (II) bipyridyl complexes, J. Phys. Chem. C 113 (2009) 7962–7969, http://dx.doi.org/10.1021/jp900842e.

[16] M.E. Strayer, J.M. Binz, M. Tanase, S.M. Kamali Shahri, R. Sharma, R.M. Rioux, T.E. Mallouk, Interfacial bonding stabilizes rhodium and rhodium oxide nanoparticles on layered Nb oxide and Ta oxide supports, J. Am. Chem. Soc. 136 (2014) 5687–5696, http://dx.doi.org/10.1021/ja412933k.

[17] J. Sun, L. Liu, X. Zhao, S. Yang, S. Komarneni, D. Yang, Capture of radioactive cations from water using niobate nanomaterials with layered and tunnel structures, RSC Adv. 5 (2015) 75354–75359, http://dx.doi.org/10.1039/C5RA10907H.

[18] J. Sun, D. Yang, C. Sun, L. Liu, S. Yang, Y. Alec Jia, R. Cai, X. Yao, Potassium niobate nanolamina: a promising adsorbent for entrapment of radioactive cations from water, Sci. Rep. 4 (2014) 7313, http://dx.doi.org/10.1038/srep07313.

[19] B.C. Viana, O.P. Ferreira, A.G.S. Filho, A.A. Hidalgo, J.M. Filho, O.L. Alves, Alkali metal intercalated titanate nanotubes: a vibrational spectroscopy study, Vib. Spectrosc. 55 (2011) 183–187, http://dx.doi.org/10.1016/j.vibspec.2010.11.007.

[20] O.P. Ferreira, A.G. Souza Filho, J. Mendes Filho, O.L. Alves, Unveiling the structure and composition of titanium oxide nanotubes through ion exchange chemical reactions and thermal decomposition processes, J. Braz. Chem. Soc. 17 (2006) 393–402, http://dx.doi.org/10.1590/S0103-50532006000200025.

[21] X. Sun, Y. Li, Synthesis and characterization of ion-exchangeable titanate nanotubes, Chemistry 9 (2003) 2229–2238, http://dx.doi.org/10.1002/chem.200204394.

[22] E.A. Josepha, S. Farooq, C.M. Mitchell, J.B. Wiley, Synthesis and thermal stability studies of a series of metastable Dion–Jacobson double-layered neodymium-niobate perovskites, J. Solid State Chem. 216 (2014) 85–90, http://dx.doi.org/10.1016/j.jssc.2014.04.024.

[23] R. Dong, N.-n. Wang, Y. Wang, Y.-x. Lan, J.-s. Hu, J. He, Structure and photocatalytic performance of K1−3x M x TiNbO5 (M = Fe, Ce) for ethyl mercaptan, Russ. J. Appl. Chem. 87 (2014) 1474–1480, http://dx.doi.org/10.1134/S1070427214100139.

[24] N. Xu, T. Takei, A. Miura, N. Kumada, K.-i. Katsumata, N. Matsushita, K. Okada, Study on the effect of Pt intercalation into layered niobate perovskite for photocatalytic behavior, langmuir, ACS J. surfaces colloids 31 (2015) 7660–7665, http://dx.doi.org/10.1021/acs.langmuir.5b01958.

[25] N. Xu, T. Takei, A. Miura, N. Kumada, Preparation and phase transformation of Ag or Bi ion-exchanged layered niobate perovskite and their photocatalytic properties, J. Ceram. Soc. Jpn. 123 (2015) 690–694, http://dx.doi.org/10.2109/jcersj2.123.690.

[26] N.M. dos Santos, J.M. Rocha, J.M.E. Matos, O.P. Ferreira, J.M. Filho, B.C. Viana, A.C. Oliveira, Metal cations intercalated titanate nanotubes as catalysts for α,β unsaturated esters production, Appl. Catal. A General 454 (2013) 74–80, http://dx.doi.org/10.1016/j.apcata.2012.12.035.

[27] M. Zarei-Chaleshtori, V. Correa, N. López, M. Ramos, R. Edalatpour, N. Rondeau, R.R. Chianelli, Synthesis and evaluation of porous semiconductor hexaniobate nanotubes for photolysis of organic dyes in wastewater, Catalysts 4 (2014) 346–355, http://dx.doi.org/10.3390/catal4040346.

[28] D. Li, Q. Li, J. He, L. Hu, J. Hu, Niobate nanoscroll composite with Fe2O3 particles under moderate conditions: assembly and application research, New J. Chem. 40 (2016) 136–143, http://dx.doi.org/10.1039/C5NJ02120K.

[29] C. Hu, L. Zhang, J. Zhang, L. Cheng, Z. Zhai, J. Chen, W. Hou, Template-free method to prepare porous Cu-containing nanotubes with a good catalytic performance for styrene epoxidation, Appl. Surf. Sci. 298 (2014) 116–124, http://dx.doi.org/10.1016/j.apsusc.2014.01.137.

[30] X. Kong, Z. Guo, Q. Lu, J. Huang, L. Cao, L. Yin, J. Li, Q. Feng, Platelike Ag2Nb4O11 mesocrystals: soft chemical synthesis, formation mechanism and enhanced photocatalytic performance, J. Alloys Compd. 686 (2016) 48–54, http://dx.doi.org/10.1016/j.jallcom.2016.05.285.

[31] I.I. Kindrat, B.V. Padlyak, S. Mahlik, B. Kukliński, Y.O. Kulyk, Spectroscopic properties of the Ce-doped borate glasses, Opt. Mater. 59 (2016) 20–27, http://dx.doi.org/10.1016/j.optmat.2016.03.053.

[32] L. Zhang, Q. Li, Y. Qin, X. Zhang, X. Gao, L. Song, Investigation on the mechanism of adsorption and desorption behavior in cerium ions modified Y-type zeolite and improved hydrocarbons conversion, J. Rare Earths 34 (2016) 1221–1227, http://dx.doi.org/10.1016/S1002-0721(16)60157-6.

[33] B.C.H. Steele, Mass transport in materials incorporated in electrochemical energy conversion systems, Solid State Ionics 12 (1984) 391–406, http://dx.doi.org/10.1016/0167-2738(84)90170-X.

[34] J.G. McCarty, H. Wise, Perovskite catalysts for methane combustion, Catal. Today 8 (1990) 231–248, http://dx.doi.org/10.1016/0920-5861(90)87020-4.

[35] M. Mogensen, N.M. Sammes, G.A. Tompsett, Physical, chemical and electrochemical properties of pure and doped ceria, Solid State Ionics 129 (2000) 63–94, http://dx.doi.org/10.1016/S0167-2738 (99) 00318–5.

[36] G. Martinelli, M.C. Carotta, M. Ferroni, Y. Sadaoka, E. Traversa, Screen-printed perovskite-type thick films as gas sensors for environmental monitoring, Sensors Actuators B Chem. 55 (1999) 99–110, http://dx.doi.org/10.1016/S0925-4005(99)00054–4.

[37] A. Walkenhorst, M. Schmitt, H. Adrian, K. Petersen, CeO2: an alternative insulator material for superconducting field effect devices, Appl. Phys. Lett. 64 (1994) 1871–1873, http://dx.doi.org/10.1063/1.111783.

[38] M. Hirano, K. Minagawa, Solid solution nanocrystals in the CeO2-Y3NbO7 system: hydrothermal formation and control of crystallite growth of ceria, J. Am. Ceram. Soc. 97 (2014) 3800–3806, http://dx.doi.org/10.1111/jace.13215.

[39] B.C. Viana, O.P. Ferreira, A.G. Souza Filho, C.M. Rodrigues, S.G. Moraes, J. Mendes Filho, O.L. Alves, Decorating titanate nanotubes with CeO2 nanoparticles, J. Phys. Chem. C 113 (2009) 20234–20239, http://dx.doi.org/10.1021/jp9068043.

[40] H. Jin, N. Wang, L. Xu, S. Hou, Synthesis and conductivity of cerium oxide nanoparticles, Mater. Lett. 64 (2010) 1254–1256, http://dx.doi.org/10.1016/j.matlet.2010.02.062.

[41] Y. Liu, P. Fang, Y. Cheng, Y. Gao, F. Chen, Z. Liu, Y. Dai, Study on enhanced photocatalytic performance of cerium doped TiO2-based nanosheets, Chem. Eng. J. 219 (2013) 478–485, http://dx.doi.org/10.1016/j.cej.2012.12.098.

[42] S. Phokha, S. Pinitsoontorn, P. Chirawatkul, Y. Poo-arporn, S. Maensiri, Synthesis, characterization, and magnetic properties of monodisperse CeO2 nanospheres prepared by PVP-assisted hydrothermal method, Nanoscale Res. Lett. 7 (2012) 425, http://dx.doi.org/10.1186/1556-276X-7-425.

[43] X. Chen, S. Cao, X. Weng, H. Wang, Z. Wu, Effects of morphology and structure of titanate supports on the performance of ceria in selective catalytic reduction of NO, Catal. Commun. 26 (2012) 178–182, http://dx.doi.org/10.1016/j.catcom.2012.05.019.

[44] X. Chen, H. Wang, Z. Wu, Y. Liu, X. Weng, Novel H2Ti12O25-confined CeO2 catalyst with remarkable resistance to alkali poisoning based on the “shell protection effect, J. Phys. Chem. C 115 (2011) 17479–17484, http://dx.doi.org/10.1021/jp205069w.

[45] H. Wang, S. Cao, C. Cen, X. Chen, Z. Wu, Structure–activity relationship of titanate nanotube-confined ceria catalysts in selective catalytic reduction of NO with ammonia, Catal. Lett. 143 (2013) 1312–1318, http://dx.doi.org/10.1007/s10562-013-1084-5.

[46] X. Gu, F. Chen, B. Zhao, J. Zhang, Photocatalytic reactivity of Ce-intercalated layered titanate prepared with a hybrid method based on ion-exchange and thermal treatment, Superlattices Microstruct. 50 (2011) 107–118, http://dx.doi.org/10.1016/j.spmi.2011.05.007.

[47] I.O. Mazali, B.C. Viana, O.L. Alves, J. Mendes Filho, A.G. Souza Filho, Structural and vibrational properties of nanocrystals, J. Phys. Chem. Solids 68 (2007) 622–627, http://dx.doi.org/10.1016/j.jpcs.2007.02.001.

[48] R.K. Hailstone, A.G. DiFrancesco, J.G. Leong, T.D. Allston, K.J. Reed, A study of lattice expansion in CeO2 nanoparticles by transmission electron microscopy, J. Phys. Chem. C, Nanomater. interfaces 113 (2009) 15155–15159, http://dx.doi.org/10.1021/jp903468m.
[49] A. Ikeda-Ohno, C. Hennig, S. Weiss, T. Yaita, G. Bernhard, Hydrolysis of tetravalent cerium for a simple route to nanocrystalline cerium dioxide: an in situ spectroscopic study of nanocrystal evolution, Chemistry–A Eur. J. 19 (2013) 7348–7360, http://dx.doi.org/10.1002/chem.20120410.
[50] F. Zhang, S.-W. Chan, J.E. Spanier, E. Apak, Q. Jin, R.D. Robinson, I.P. Herman, Cerium oxide nanoparticles: size-selective formation and structure analysis, Appl. Phys. Lett. 80 (2002) 127–129, http://dx.doi.org/10.1063/1.1430502.
[51] T.M.F. Marques, O.P. Ferreira, J.A.P. da Costa, K. Fujisawa, M. Terrones, B.C. Viana, Study of the growth of CeO2 nanoparticles onto titanate nanotubes, J. Phys. Chem. Solids 87 (2015) 213–220, http://dx.doi.org/10.1016/j.jpcs.2015.08.022.
[52] L. Yu, Y. Ma, C.N. Ong, J. Xie, Y. Liu, Rapid adsorption removal of arsenate by hydrous cerium oxide-graphene composite, RSC Adv. 5 (2015) 64983–64990, http://dx.doi.org/10.1039/C5RA08922K.
[53] R.J. Packer, E.V. Tsipis, C.N. Munnings, V.V. Kharton, S.J. Skinner, J.R. Frade, Diffusion and conductivity properties of cerium niobate, Solid State Ionics 177 (2006) 2059–2064, http://dx.doi.org/10.1016/j.ssi.2006.03.044.
[54] Y. Liu, Z. Yang, H. Yu, S. Zhan, M. Cai, X. Yang, Y. Yu, Facile fabrication of cerium niobate nano-crystalline fibers by electrospinning technology, J. Sol-Gel Sci. Technol. 58 (2011) 394–399, http://dx.doi.org/10.1007/s10971-011-2405-z.
[55] J.G. Thompson, R.L. Withers, F.J. Brink, Modulated structures in oxidized cerium niobates, J. Solid State Chem. 143 (1999) 122–131, http://dx.doi.org/10.1006/jssc.1998.8096.
[56] F. Vullum, T. Grande, Oxygen stoichiometry and transport properties of cerium niobate, Solid State Ionics 179 (2008) 1061–1065, http://dx.doi.org/10.1016/j.ssi.2007.12.079.
[57] G. Zhang, W. Wan, P. Long, Q. Li, C. Deng, Z. Yi, Synthesis and characterization of mixed conductor CeNbO4, J. Alloys Compd. 616 (2014) 328–332, http://dx.doi.org/10.1016/j.jallcom.2014.05.229.
[58] S. Kato, M. Ammann, T. Huthwelker, C. Paun, M. Lampimaki, M.-T. Lee, M. Rothensteiner, J.A. van Bokhoven, Quantitative depth profiling of Ce3+ in Pt/CeO2 by in situ high-energy XPS in a hydrogen atmosphere, Phys. Chem. Chem. Phys. 17 (2015) 5078–5083, http://dx.doi.org/10.1039/C4CP05643D.
[59] A.L. Shiguihara, M.A. Bizeto, V.R.L. Constantino, Chemical modification of niobium layered oxide by tetraalkylammonium intercalation, J. Braz. Chem. Soc. 21 (2010) 1366–1376.
[60] L. Wang, Y. Omomo, N. Sakai, K. Fukuda, I. Nakai, Y. Ebina, K. Takada, M. Watanabe, T. Sasaki, Fabrication and characterization of multilayer ultrathin films of exfoliated MnO2 nanosheets and polycations, Chem. Mater. 15 (2003) 2873–2878, http://dx.doi.org/10.1021/cm034191r.
[61] A.L. Shiguihara, M.A. Bizeto, V.R.L. Constantino, Exfoliation of layered hexaniobate in tetra(n-butyl)ammonium hydroxide aqueous solution, Colloids Surfaces A Physicochem. Eng. Aspects 295 (2007) 123–129, http://dx.doi.org/10.1016/j.colsurfa.2006.08.040.
[62] H. Wilkens, O. Schuckmann, R. Oelke, S. Gevers, M. Reichling, A. Schaefer, M. Baumer, M.H. Zoellner, G. Niu, T. Schroeder, J. Wollschlager, Structural transitions of epitaxial ceria films on Si(111), Phys. Chem. Chem. Phys. 15 (2013) 18589–18599, http://dx.doi.org/10.1039/C3CP52688G.
[63] M.Z. Atashbar, H.T. Sun, B. Gong, W. Wlodarski, R. Lamb, XPS study of Nb-doped oxygen sensing TiO2 thin films prepared by sol-gel method, Thin Solid Films 326 (1998) 238–244, http://dx.doi.org/10.1016/S0040-6090(98) 00534–3.
[64] N. Özer, D.-G. Chen, C.M. Lampert, Preparation and properties of spin-coated Nb2O5 films by the sol-gel process for electrochromic applications, Thin Solid Films 277 (1996) 162–168, http://dx.doi.org/10.1016/0040-6090(95)08011-2.
[65] T. Hryniewicz, K. Rokosz, H.R.Z. Sandim, SEM/EDX and XPS studies of niobium after electropolishing, Appl. Surf. Sci. 263 (2012) 357–361, http://dx.doi.org/10.1016/j.apsusc.2012.09.060.
[66] M. Romeo, K. Bak, J. El Fallah, F. Le Normand, L. Hilaire, XPS Study of the reduction of cerium dioxide, Surf. Interface Anal. 20 (1993) 508–512, http://dx.doi.org/10.1002/sia.740200604.
[67] A. Pereira, M. Blouin, A. Pillonnet, D. Guay, Structure and valence properties of ceria films synthesized by laser ablation under reducing atmosphere, Mater. Res. Express 1 (2014) 015704, 2053-1591/1/i=1/a=015704.